Nano Research

Open Access

Research Article

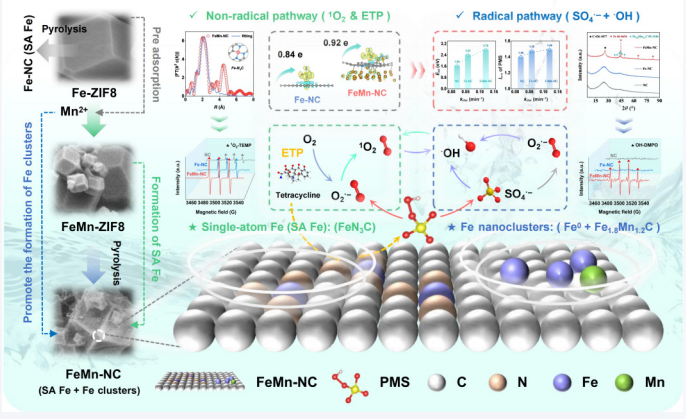
Peroxymonosulfate activation on dual iron sites for efficient antibiotic degradation: Synergistic effects of single-atom iron and iron nanoclusters

Wangbo Wang, Ting Wu, Jing Li, Dongsheng Zhang, Chenxi Li, Xiaohan Du, and Weihuang Zhu ✉

Key Laboratory of Northwest Water Resources, Environment and Ecology, Ministry of Education, Xi'an University of Architecture and Technology, Xi'an 710055, China

Cite this article: *Nano Research*, **2026**, *19*, 94908780. https://doi.org/10.26599/NR.2026.94908780

ABSTRACT: Single-atom catalysts (SACs) have emerged as a promising frontier in Fenton-like processes. However, optimizing their isolated and dispersed active sites remains a major challenge. Herein, a Mn-modulated dual-Fe-site catalyst (FeMn-NC) featuring both Fe single atoms and Fe nanoclusters was developed. Mn incorporation promoted the formation of Fe nanoclusters composed of Fe^0 and $Fe_{1.8}Mn_{1.2}C$ species. The catalyst achieved 97.1% tetracycline (TC) degradation via peroxymonosulfate (PMS) activation, with a reaction rate constant (k) of 0.1152 min^{-1}, arising from the synergistic interplay between Fe single atoms and Fe nanoclusters. Mechanistically, Fe single atoms dominated the non-radical pathway, whereas Fe nanoclusters enhanced electron transfer and introduced a complementary radical route. Density functional theory (DFT) calculations revealed that the coexistence of Fe single atoms and Fe nanoclusters optimized charge distribution and the Fe d-band center, thereby enhancing electron delocalization and promoting PMS adsorption, O–O bond activation, and interfacial Bader charge transfer. Additionally, Fukui function calculation, intermediate products analysis, and wheat germination assays confirmed the reduced environmental toxicity of pollutants after catalytic degradation. This work provides new insights into the rational design of SACs with multiple active sites for the efficient catalytic PMS activation.



KEYWORDS: single-atom Fe, Fe nanoclusters, Mn modulation, peroxymonosulfate activation, antibiotic wastewater purification

1 Introduction

As emerging contaminants, antibiotics exert a well-documented detrimental impact on public health and ecosystems [1, 2]. The Fenton reaction has emerged as an efficient and straightforward solution for antibiotic degradation [3–5]. Within the research area of advanced oxidation processes, peroxymonosulfate (PMS)-activated systems have been extensively investigated due to their robust reactive oxidation species (ROS) generation capability, underscoring their utility in wastewater treatment applications [6, 7].

Received: March 14, 2026; **Revised:** April 21, 2026
Accepted: April 27, 2026

✉Address correspondence to zhuweihuang@xauat.edu.cn

However, the slow decomposition kinetics of peroxide bond in PMS molecules limit its practical application, thus, the effective PMS activation methods should be developed to enhance the yield of ROS [8, 9]. Current strategies for PMS activation can be broadly categorized into thermal, radiative, transition metal-based, carbon-based, and alkaline approaches [10]. Among these, transition metal-based catalysts are particularly attractive due to their cost-effectiveness, environmental benignity, and high activation capability; however, their practical application is often limited by particle agglomeration, metal leaching, and low PMS utilization efficiency [11, 12]. Therefore, the development of transition metal catalysts with enhanced dispersibility, improved stability, and superior degradation performance represents a crucial challenge in persulfate activation for antibiotic wastewater treatment.

Single-atom catalysts (SACs), with their multifunctionality in

generating ROS, forming high-valent metal-oxo species, and mediating electron transfer, have thus emerged as an ideal candidate for PMS activation [13–15]. SACs with structures such as Fe-pyridinic N_4 can synergistically enhance PMS activation by inducing electron-deficient regions in adjacent carbon atoms [16]. Also, adjusting spacing between adjacent Fe sites enhances electronic interaction and cooperative adsorption, improving stability and efficiency [17]. Moreover, unsaturated coordination (e.g., FeN_3) further boosts activity by elevating local electron density and optimizing PMS interaction, accelerating high-valent Fe species formation [18]. Additionally, multi-heteroatom designs (e.g., axial O and second-shell P doping) enable synergistic PMS adsorption and intermediate desorption, promoting selective $^1O_2$ generation with high adaptability [19]. Despite these advances, conventional single-atom catalysts still face challenges such as low metal loading, limited active-site diversity, and insufficient stability, hindering their practical application in wastewater treatment [20, 21].

The coexistence of single atoms and nanoclusters provides complementary active sites and enhances electronic interactions, collectively improving charge transfer and steering ROS reaction pathways for efficient PMS activation [22, 23]. For example, Fe nanoclusters with atomic sites promote adsorption-driven PMS activation, while Fe-N_4 centers alongside particles favor charge redistribution and non-radical pathways [24, 25]. When aligned vertically in three-dimensional (3D) carbon frameworks, these synergistic structures drive cooperative electron transfer, yielding both radical and non-radical oxidants with enhanced stability [26]. In systems like CoNPs-SAs@N-C, encapsulated particles further enhance mass transport and intensify electronic interactions at atomic sites, boosting singlet oxygen generation and catalytic durability [27]. Moreover, iron nanoclusters modulate Fe-N_4 sites through a remote effect, lowering the reaction barrier and enhancing the reaction kinetics [28]. Therefore, the deliberate integration of single atoms with nanoclusters represents an intrinsic strategy for tailoring the electronic structure of active sites and enabling the development of efficient, adaptable, and stable PMS-activating catalysts. Nevertheless, the controlled coexistence of these two distinct sites within a single catalyst remains challenging, as straightforward and reliable synthetic routes for constructing such synergistic systems are still scarce.

Therefore, a Mn-modified dual Fe-site catalyst (FeMn-NC) was designed to activate PMS for enhanced tetracycline (TC) degradation. It exhibited high catalytic performance, which was systematically correlated with its structural characteristics, reaction kinetics, and stability. The reaction mechanism was elucidated through electrochemical characterization, ROS quenching experiments, and electron paramagnetic resonance (EPR) spectroscopy. The degradation pathways of TC and its environmental impact were further investigated via liquid chromatography-mass spectrometry (LC-MS) and toxicity evaluation. All experimental observations were supported by density functional theory (DFT) calculations. This study provides valuable design insights for the development of efficient and low-cost dual-site catalysts featuring synergistic single-atom and nanocluster configurations for the removal of emerging contaminants from wastewater.

2 Experimental

2.1 Materials and chemicals

Tetracycline antibiotics, including TC (99%), oxytetracycline (OTC, 99%), and chlortetracycline (CTC, 99%), as well as organic dyes such as rhodamine B (RhB, 99%), methylene blue (MB, 99%), and orange G (OG, 99%), were obtained from Macklin Biochemical Co., Ltd., Shanghai, China. Potassium peroxymonosulfate (PMS, ≥ 47%) and the ligand precursor 2-methylimidazole (HMeIM, 99%) were also purchased from the same supplier. Other reagents, including potassium hydroxide, ferric acetylacetonate ($Fe(acac)_3$, 99%), manganese(II) chloride tetrahydrate ($MnCl_2{\cdot}4H_2O$, 99%), zinc nitrate hexahydrate ($Zn(NO_3)_2{\cdot}6H_2O$, 99%), mineral acids (HCl, 99%; H_2SO_4, 99%), and inorganic salts (NaCl, 99%; $NaHCO_3$, 99%; $NaNO_3$, 99%; NaH_2PO_4, 99%), were purchased from Tianli Chemical Reagent Co., Ltd., Tianjin, China. Additionally, p-benzoquinone (p-BQ, 98%), L-histidine (99%), and anhydrous organic solvents—ethanol (EtOH, 99%), methanol (MeOH, 99%), and tert-butanol (TBA, 99%)—were obtained from the same supplier. Radical spin-trapping reagents, 2,2,6,6-tetramethyl-piperidine (TEMP), and 5,5-dimethyl-1-pyrroline N-oxide (DMPO), each of 99% purity, were sourced from Sigma-Aldrich (USA). All chemicals were used as received. Deionized water was used for the preparation of all aqueous solutions.

2.2 Synthetic strategy

$Zn(NO_3)_2{\cdot}6H_2O$, $MnCl_2{\cdot}4H_2O$, and $Fe(acac)_3$ were dissolved in methanol and combined with a separate methanolic solution of 2-methylimidazole. The mixture was vigorously stirred at room temperature for 12 h. The resulting precipitate was collected by centrifugation, washed three times with methanol, and vacuum-dried at 60 °C for 12 h. The obtained powder, denoted as FeMn-ZIF8, was pyrolyzed under a flowing N_2 atmosphere at 800, 900, or 1000 °C for 2 h with a heating rate of 5 °C·min^{-1} (Fig. 1(a)). For comparison, NC, Mn-NC, and Fe-NC were prepared by direct pyrolysis of ZIF-8, Mn-ZIF8, and Fe-ZIF8, respectively, under identical conditions.

2.3 Characterizations

Catalysts were characterized by scanning electron microscopy (SEM, JSM-6510LV), high-resolution transmission electron microscopy (HR-TEM, FEI Talos F200x), and X-ray diffraction (XRD, Shimadzu Ultima IV). The surface composition and valence states were analyzed by X-ray photoelectron spectroscopy (XPS, K-Alpha). X-ray absorption fine structure (XAFS, Singapore Synchrotron Light Source) was used to investigate the coordination environment and oxidation states of the single-atom catalysts. Functional groups were characterized using Fourier-transform infrared (FTIR) spectroscopy (Shimadzu IRTracer-10) and Raman spectroscopy (Horiba LabRAM HR Evolution). Textural properties were obtained from N_2 adsorption–desorption (ASAP 2460) via Brunauer–Emmett–Teller (BET) analysis. Pollutant concentration was quantified by UV–visible spectrophotometry (Shimadzu UV-1780) at 357 nm. Total organic carbon (TOC) content was measured on a Shimadzu TOC‑L analyzer. Leached iron ions were quantified by inductively coupled plasma-mass spectrometry (ICP-MS, Agilent 7800). All electrochemical measurements, including cyclic voltammetry (CV), chronoamperometry (*i*–*t*), and linear sweep voltammetry (LSV), were conducted using a CHI600E electrochemical workstation. A standard three-electrode configuration was employed in a 100 mM Na_2SO_4 electrolyte solution [29]. EPR spectra (EMX micro) were recorded at 3500 G using TEMP and DMPO to detect $^1O_2$ and $SO_4^{\cdot-}$/·OH radicals, respectively.

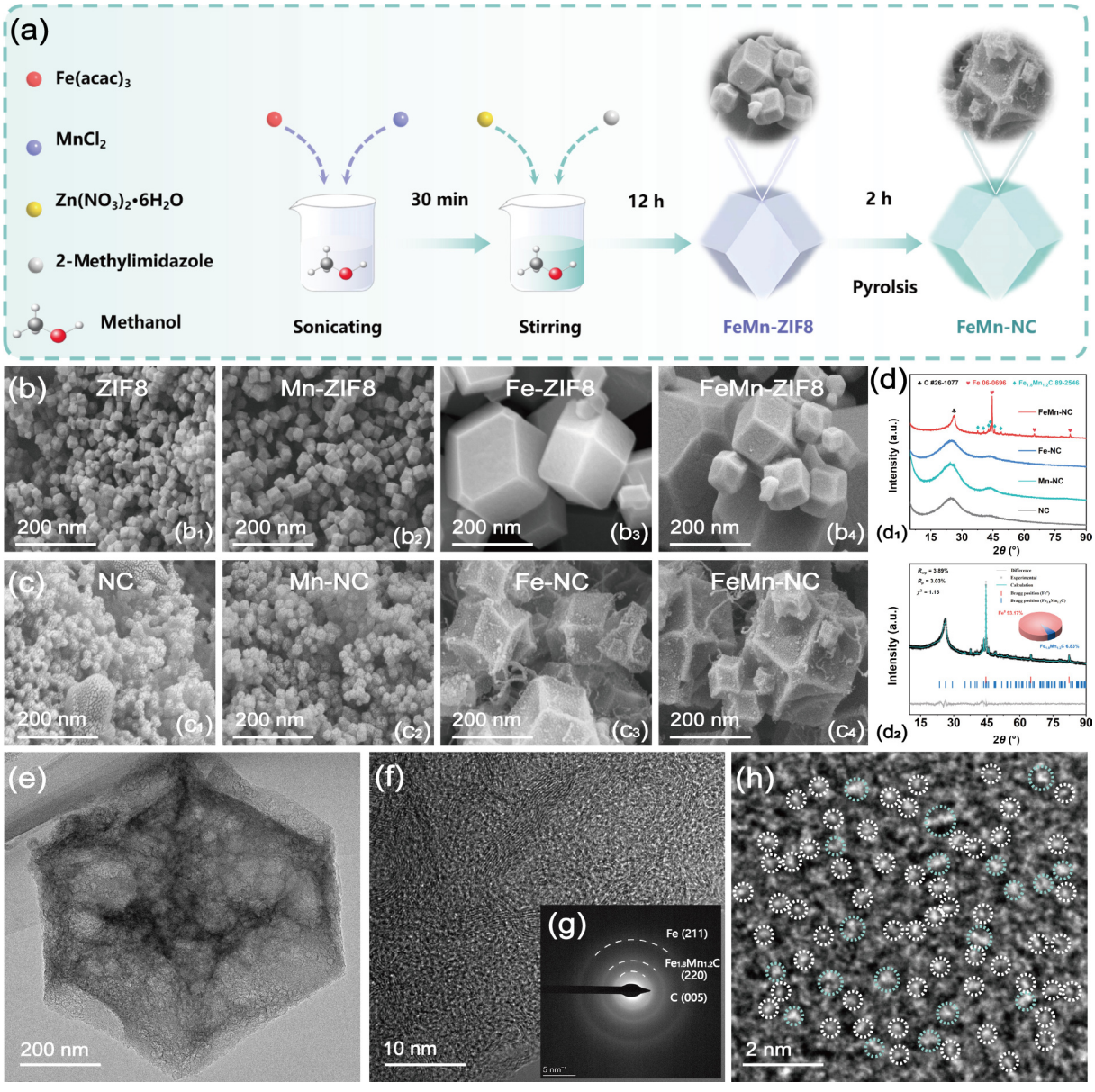


Figure 1 (a) Schematic synthetic illustration of FeMn-NC. (b_1)–(b_4) SEM images of ZIF8, Mn-ZIF8, Fe-ZIF8, and FeMn-ZIF8. (c_1)–(c_4) SEM images of N/C, Mn-N/C, Fe-N/C, and FeMn-N/C. (d_1) XRD characterization of N/C, Mn-N/C, Fe-N/C, and FeMn-N/C and (d_2) Rietveld refinement for the diffraction pattern of FeMn-NC containing Fe nanoclusters composed of Fe^0 and $Fe_{1.8}Mn_{1.2}C$. (e), (f), and (h) TEM images of FeMn-NC. (g) SAED pattern of FeMn-NC.

2.4 Degradation experiments

The degradation experiment was initiated by adding PMS and catalyst into 50 mL of 0.1 mM pollutant solution under continuous stirring. The activation energy (E_a) and reaction rate constant (k) were derived from concentration data, which were obtained by sampling the reaction mixture at predetermined time points and applying Eqs. (1) and (2) [7]

$$-\ln\left(\frac{c_t}{c_0}\right) = kt \quad (1)$$

$$\ln k = -\frac{E_a}{RT} + \ln A \quad (2)$$

For kinetic analysis, C_0 and C_t denoted the initial and time-dependent pollutant concentrations, respectively, while T, R, and A represented the reaction temperature, universal gas constant, and pre-exponential factor [30].

3 Results and discussion

3.1 Characterizations

SEM imaging confirmed the formation of precursor particles with a rhombic dodecahedron morphology for ZIF8, Fe-ZIF8, Mn-ZIF8, and FeMn-ZIF8 [31]. Notably, the FeMn-ZIF8 particles exhibited a larger average size and a greater degree of size heterogeneity compared to the other samples, particularly Fe-ZIF8. Importantly, this dodecahedral framework was well-preserved in FeMn-NC even after pyrolysis at 1000°C (Figs. 1(b) and 1(c)). Energy dispersive X-ray spectroscopy (EDS) revealed a uniform dispersion of C, N, and Fe within the FeMn-NC structure, confirming successful Fe

incorporation into the N-doped carbon framework without aggregation. Also, TEM images showed no discernible nanoparticles or lattice fringes, indicating that Fe species were primarily dispersed as single atoms on the carbon support. The corresponding selected area electron diffraction (SAED) pattern exhibited diffuse diffraction rings, which were indexed to the (005), (211), and (220) crystallographic planes of carbon, Fe^0, and $Fe_{1.8}Mn_{1.2}C$, respectively [32].

The XRD characterization of NC, Mn-NC, and Fe-NC catalysts (Fig. 1(d_1)) exhibited similar structural features, with no distinct peaks corresponding to iron carbides or oxides. However, the introduction of manganese in FeMn-NC led to the emergence of definitive peaks for Fe^0 and the concomitant formation of $Fe_{1.8}Mn_{1.2}C$. Quantitative Rietveld refinement confirmed the phase composition to be 93.17% Fe^0 and 6.83% $Fe_{1.8}Mn_{1.2}C$ (Fig. 1(d_2)).

XPS analysis revealed no detectable Fe^{2+} or Fe^{3+} signals in the Fe 2p spectra of all catalysts (NC, Mn-NC, Fe-NC, and FeMn-NC), primarily due to the low Fe doping content (Fig. S4(b) in the Electronic Supplementary Material (ESM)). A weak Fe^0 peak was detected in FeMn-NC but not in Fe-NC, indicating that Mn introduction facilitated the reduction of Fe species. Analysis of the C 1s XPS spectra revealed that the C–N peak of FeMn-NC confirmed an increased degree of graphitization (Fig. 2(a)). Similarly, the N 1s spectra showed that, compared with other control samples, both graphitic nitrogen and Fe–N content in FeMn-NC were increased (Fig. 2(b)). Similarly, the enhanced Fe–N signal further supported the successful anchoring of iron single atoms. In the O 1s high-resolution spectrum (Fig. 2(c)), the oxygen vacancy content in FeMn-NC was 57.4%, significantly higher than that in other control samples, while the lattice oxygen content was only 7.9%, collectively suggesting a higher defect density and lower iron oxide crystallinity in FeMn-NC.

X-ray absorption near-edge structure (XANES) and extended X-ray absorption fine structure (EXAFS) measurements were conducted to probe the immediate atomic environment surrounding iron species. According to the Fe K-edge XANES data (Fig. 2(d)), the average Fe oxidation state in FeMn-NC was situated between that of metallic Fe(0) and Fe_2O_3(+3). A first-shell Fe–N bond length of 1.94 Å was determined by quantitative EXAFS fitting, closely matching the 1.95 Å observed in Fe-phthalocyanine (Fe-Pc), confirming a similar Fe–N coordination environment (Table S1 in the ESM). The Fourier-transform spectrum (Fig. 2(e))

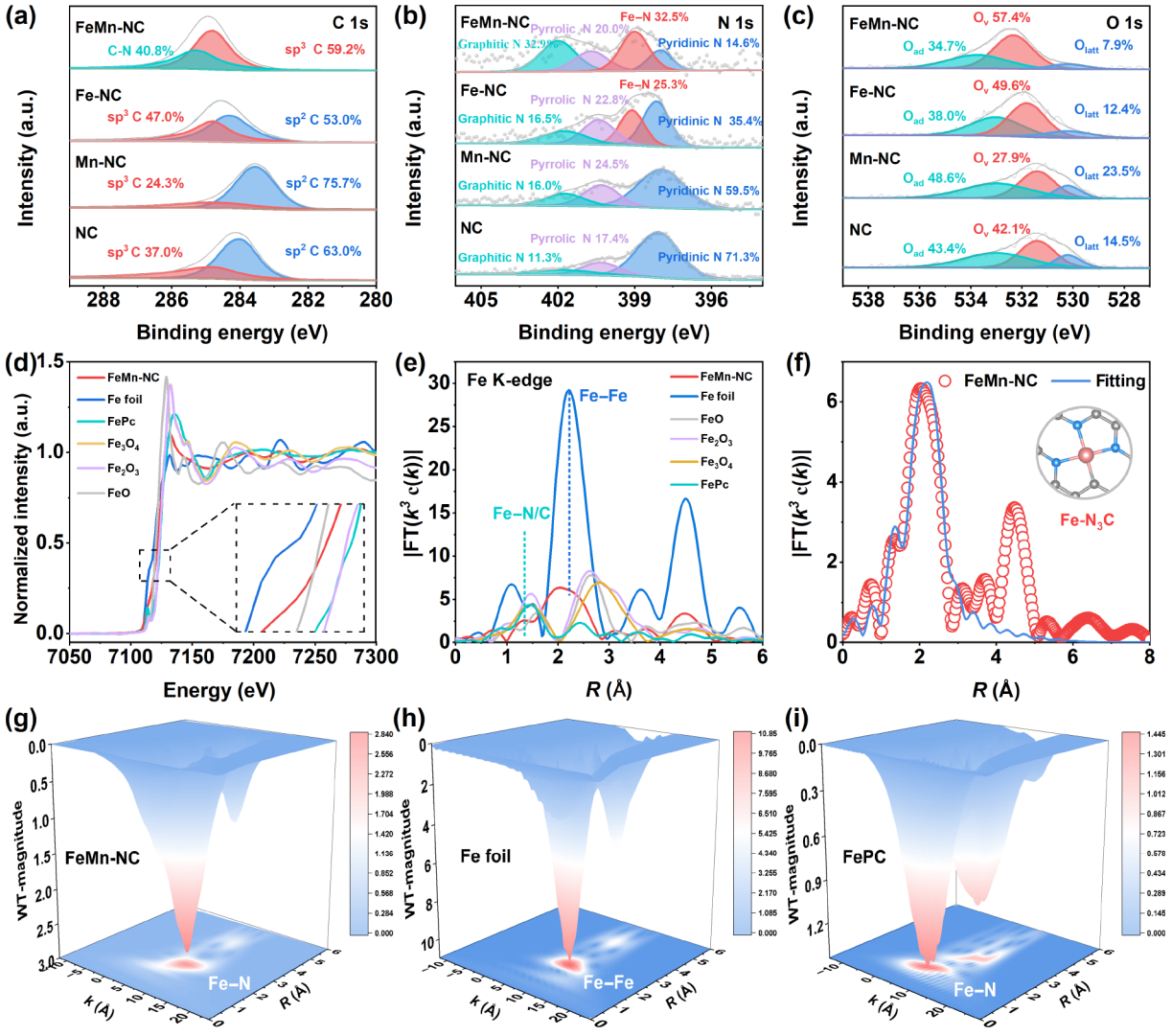


Figure 2 (a)–(c) XPS spectra of C 1s, N 1s, and O 1s of NC, Mn-NC, Fe-NC, and FeMn-NC. (d) Normalized Fe K-edge XANES spectra of FeMn-NC and the references. (e) Fe K-edge FT-EXAFS spectra of FeMn-NC and references. (f) EXAFS fitting curves of FeMn-NC in *R* space (inset is the proposed FeMn-NC architectures). (g)–(i) WT-EXAFS plots of FeMn-NC and the references.

exhibited prominent peaks at 1.34 and 2.22 Å, corresponding to the Fe–N(C) and Fe–Fe coordination shells, respectively. Notably, no Fe–O scattering path was detected, indicating the absence of iron oxides.

According to detailed fitting results (Fig. 2(f) and Figs. S6–S8 and Table S1 in the ESM), the average first-shell coordination number was 2.86 for Fe–N and 0.92 for Fe–C. These findings demonstrated that controlled pyrolysis combined with Mn doping effectively modulates the distribution of nitrogen/carbon species, enabling the precise formation of a FeN_3C coordination structure. Further evidence for the distinct coordination states was provided by wavelet transform analysis. The contour plot (Figs. 2(g)–2(i)) displayed an intensity maximum for FeMn-NC at 7.68 $Å^{-1}$. positioned between the characteristic maxima for Fe–N (7.64 $Å^{-1}$) and Fe–Fe (8.3 $Å^{-1}$) references. Based on these findings, the results provided direct evidence for the simultaneous presence of both isolated Fe atoms and Fe nanoclusters.

FTIR spectrum verified the successful preparation of the FeMn-ZIF8 precursor and indicated the absence of specific functional groups in FeMn-NC (Fig. S9 in the ESM) [33]. Furthermore, the Raman spectrum of FeMn-NC showed a lower I_D/I_G ratio compared to NC, Mn-NC, and Fe-NC, indicating a reduced defect density and enhanced graphitization (Fig. S10 in the ESM) [34]. N_2 physisorption measurements were conducted to evaluate the pore structure of FeMn-NC, along with control samples and precursors (Fig. S11 in the ESM). All adsorption–desorption isotherms exhibited Type II characteristics, indicating that the materials are primarily dominated by external surface adsorption with limited microporosity, while still facilitating rapid pollutant diffusion and exposure of active sites [35]. FeMn-NC exhibited a slightly higher specific surface area and larger pore size (~ 40 nm) than Fe-NC, enhancing the accessibility of active sites. Combined with the synergistic interplay between Fe single atoms and nanoclusters, these structural features contribute to the superior catalytic performance of FeMn-NC.

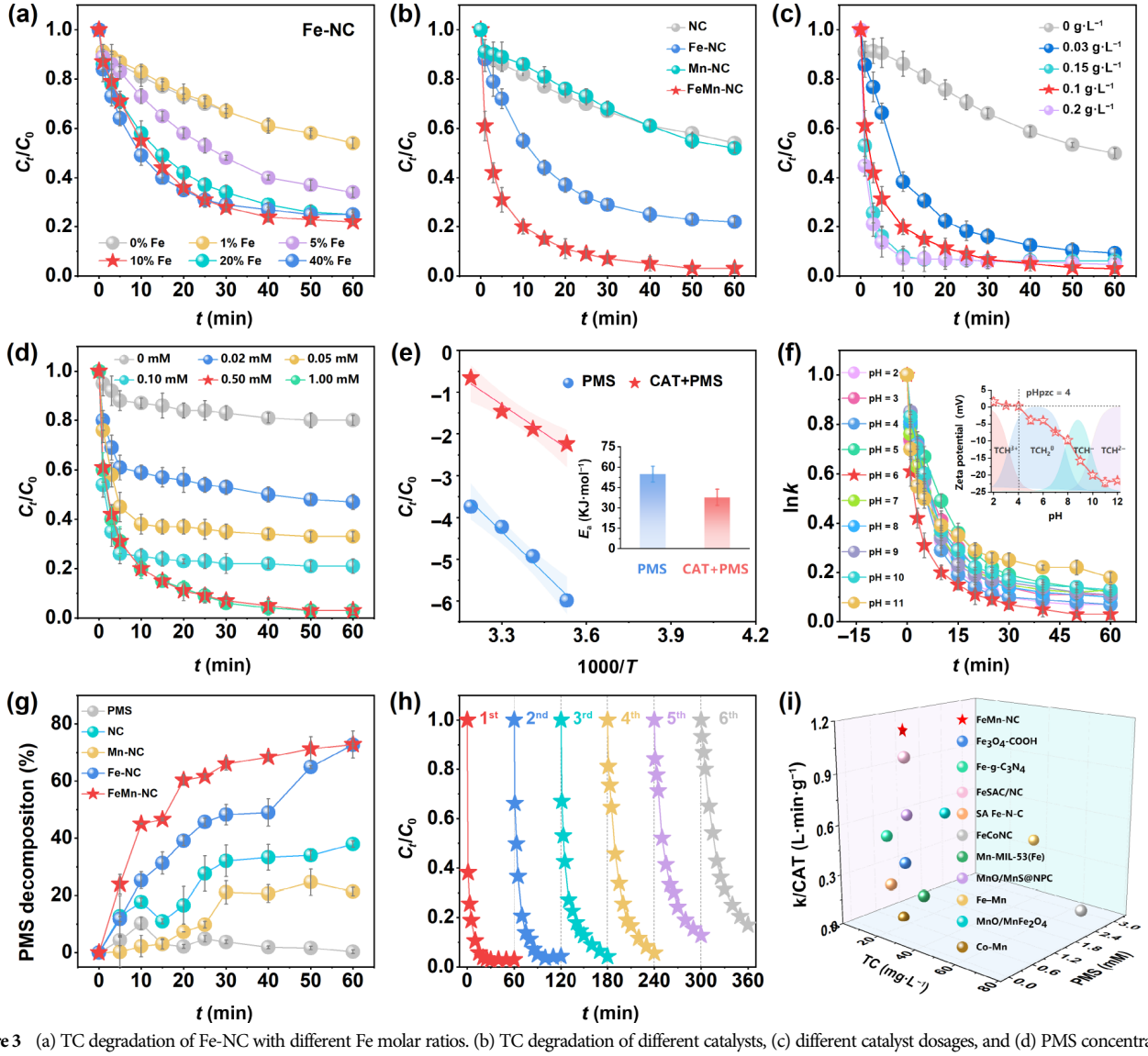


Figure 3 (a) TC degradation of Fe-NC with different Fe molar ratios. (b) TC degradation of different catalysts, (c) different catalyst dosages, and (d) PMS concentrations in the PMS/CAT system. (e) Kinetic characteristics of the PMS activation process and activation energies of only PMS and PMS + CAT (FeMn-NC). (f) Initial pH on the PMS activation performance toward TC removal and zeta potential under various pH conditions. (g) PMS decomposition efficiency of different catalysts. (h) Recycling tests on TC degradation in the PMS/FeMn-NC system. (i) Kinetic reaction rate constant comparison between FeMn-NC and the previously reported studies during the PMS activation process.

3.2 Catalytic performance

Figure 3(a) demonstrated that Fe-NC with 10% initial Fe loading exhibited optimal PMS activation for TC degradation. The TC removal efficiency in the PMS/Fe-NC system increased with pyrolysis temperature from 800 to 1000 °C (Fig. S12 in the ESM), and 1000 °C was identified as the optimal pyrolysis temperature. FeMn-NC was subsequently synthesized via a one-pot process with 10% initial Fe loading, addition of manganese chloride, and pyrolysis at 1000 °C. In the PMS activation system, FeMn-NC achieved a TC degradation efficiency of 97.1%, significantly outperforming the control samples.

As shown in Fig. 3(b) and Fig. S14 in the ESM, the PMS/FeMn-NC system delivered a high TC removal efficiency of 97.1% with the k of 0.1152 min^{-1}. FeMn-NC alone removed 23.7% of TC, whereas PMS alone resulted in 45.5% removal (Fig. 3(c)). Moreover, FeMn-NC exhibited substantial mineralization ability, achieving 55.4% TOC removal within 1 h (Table S3 in the ESM). TC removal efficiency increased with higher catalyst and PMS concentrations, although no significant improvement was observed once the catalyst concentration exceeded 0.1 $g{\cdot}L^{-1}$ or PMS concentration surpassed 0.5 mM (Figs. 3(c) and 3(d)). Overall, the superior catalytic performance was attributed to the synergy between Fe/Mn composition, pyrolysis-induced active sites, and operational parameter. As shown in Fig. S13(b) in the ESM, FeMn-NC exhibited effective PMS activation across a temperature range of 10 to 40 °C, and the TC removal efficiency increased with temperature. According to Fig. 3(e), the activation energy of the PMS/FeMn-NC system was 37.91 $kJ{\cdot}mol^{-1}$, representing a 31.06% reduction compared to the catalyst-free system. The results clearly demonstrated that FeMn-NC significantly reduced the activation energy (E_a) of the PMS decomposition process, enhanced the reaction rate, and substantially improved the PMS activation kinetics.

Under varying acidic to alkaline conditions (pH 2–11), FeMn-NC consistently achieved high efficiency in removing TC (Fig. 3(f)). Given the pH-dependent speciation of tetracycline (predominantly as TCH_3^+ at pH < 3.3, TCH_2^0 at pH 3.3–7.7, TCH^- at pH 7.7–9.7, and TC^{2-} at pH > 9.7), this performance was particularly remarkable [36]. Especially, the point of zero charge (pHpzc) for the FeMn-NC was determined to be 4.0 (Fig. 3(f)). Although electrostatic interactions between the catalyst and TC are expected to vary with pH, the removal efficiency remained consistently high across the entire pH range studied, even at values near the pHpzc. These results highlighted the ability of FeMn-NC to mitigate electrostatic repulsion on TC removal, and Figs. 3(g)–3(i) showed its high PMS decomposition, stability, and advantages.

3.3 Electron transfer and ROS identification

CV measurements indicated that FeMn-NC exhibited the largest electrochemical active surface area (ECSA) among all tested samples, with a value of 102.15 $cm^2{\cdot}g^{-1}$, due to its significant pseudo capacitance (surface redox charge storage) (Fig. 4(a)) [37]. This improvement was ascribed to the coexisting Fe^0 and single-atom Fe surface structures, which increased the number of active sites and expanded the reactive interface for electron transfer. LSV further revealed a significantly stronger current response for FeMn-NC at identical potentials (Fig. 4(b)), confirming that the synergistic effect effectively enhanced intrinsic electron conduction and accelerated interfacial charge transfer kinetics [38]. In i–t tests, FeMn-NC exhibited an immediate increase in current upon PMS addition (Fig. 4(c)), indicating that its dual-active-site structure facilitated more efficient electron transfer to PMS and enhanced ROS generation compared with single-site catalysts [39]. The subsequent current variation following TC addition confirmed the function of the catalyst in mediating electron transfer between the pollutant and oxidizer.

Open-circuit potential measurements showed that FeMn-NC maintains a higher steady-state potential (0.4 mV), demonstrating its enhanced capability to establish and sustain a stronger driving force for electron transfer (Fig. 4(d)). This interpretation was corroborated by galvanic observation procedure (GOP), where the current increased notably from 35 to 160 μA (Fig. 4(e)), confirming both the enhanced system-wide electron flux and the directional electron transfer pathway (TC → catalyst → PMS) [40]. Moreover, the k values of different catalysts showed a positive correlation with key electrochemical parameters (pseudo-capacitance, current response, and open-circuit potential), which was consistent with the trend observed for TC degradation efficiency (Figs. 4(g)–4(i)). These results provided direct evidence for the intrinsic connection between electrochemical activity and catalytic performance.

To identify the primary ROS, quenching experiments were carried out with MeOH, TBA, L-histidine, and p-BQ to quench hydroxyl radicals (·OH), sulfate radicals ($SO_4^{\cdot-}$), singlet oxygen ($^1O_2$), and superoxide radicals ($O_2^{\cdot-}$) (Figs. S20(a)–S20(d) in the ESM) [41]. Quenching experiments demonstrated that TC degradation was significantly inhibited by MeOH, TBA, and p-BQ in a concentration-dependent manner, whereas L-histidine exhibited negligible effects in the PMS/FeMn-NC system. These findings demonstrated that in the PMS/FeMn-NC system, the degradation process was predominantly driven by $SO_4^{\cdot-}$, ·OH, $^1O_2$, and $O_2^{\cdot-}$, which contributed 34.8%, 32.3%, 22.9%, and 10.0% to the overall degradation, respectively (Fig. 5(c)).

As presented in Fig. S22 in the ESM, distinct signals corresponding to ·OH and $^1O_2$ were observed within the initial 1 min of the reaction, indicating the rapid formation of these reactive species at the initial stage. The sustained signals of ·OH and $^1O_2$ observed over the following 10-min reaction period confirmed their continuous generation during PMS activation. Moreover, EPR measurements on different catalysts revealed that the FeMn-NC system showed a markedly stronger DMPO-·OH signal intensity than Fe-NC (Fig. 5(d)). This suggested that the presence of Fe^0 facilitated PMS activation, effectively enhancing ·OH generation. Furthermore, as shown in Fig. 5(e), this system also demonstrated the most prominent TEMP-$^1O_2$ signal intensity among all catalysts. This confirmed that the incorporation of Fe^0 also played a contributory role in the single-atom iron-mediated activation of PMS to generate $^1O_2$.

Under a nitrogen-saturated (N_2) atmosphere, the signal intensities of the DMPO-·OH adducts remained largely unchanged (Fig. 5(f)(4)), indicating that the conversion of ·OH via the oxygen reduction reaction pathway was insignificant. Under the same anaerobic conditions, however, a marked reduction was observed in the EPR peak intensity of the TEMP-$^1O_2$ adduct (Fig. 5(g)(4)), indicating that dissolved oxygen was crucial for $^1O_2$ formation. The addition of MeOH substantially suppressed the EPR signals of DMPO-·OH and TEMP-$^1O_2$ adducts (Figs. 5(f)(5) and 5(g)(5)), indicating that ·OH and $^1O_2$ were formed via $SO_4^{\cdot-}$-mediated pathways (Eqs. (3) and (7)). Upon the addition of TBA, the EPR signal of the DMPO-·OH adduct showed only slight attenuation (Fig. 5(f)(6)). This limited reduction can be explained by the mutual quenching reaction between $SO_4^{\cdot-}$ and ·OH in the presence of this

清华大学出版社 Tsinghua University Press | SciOpen

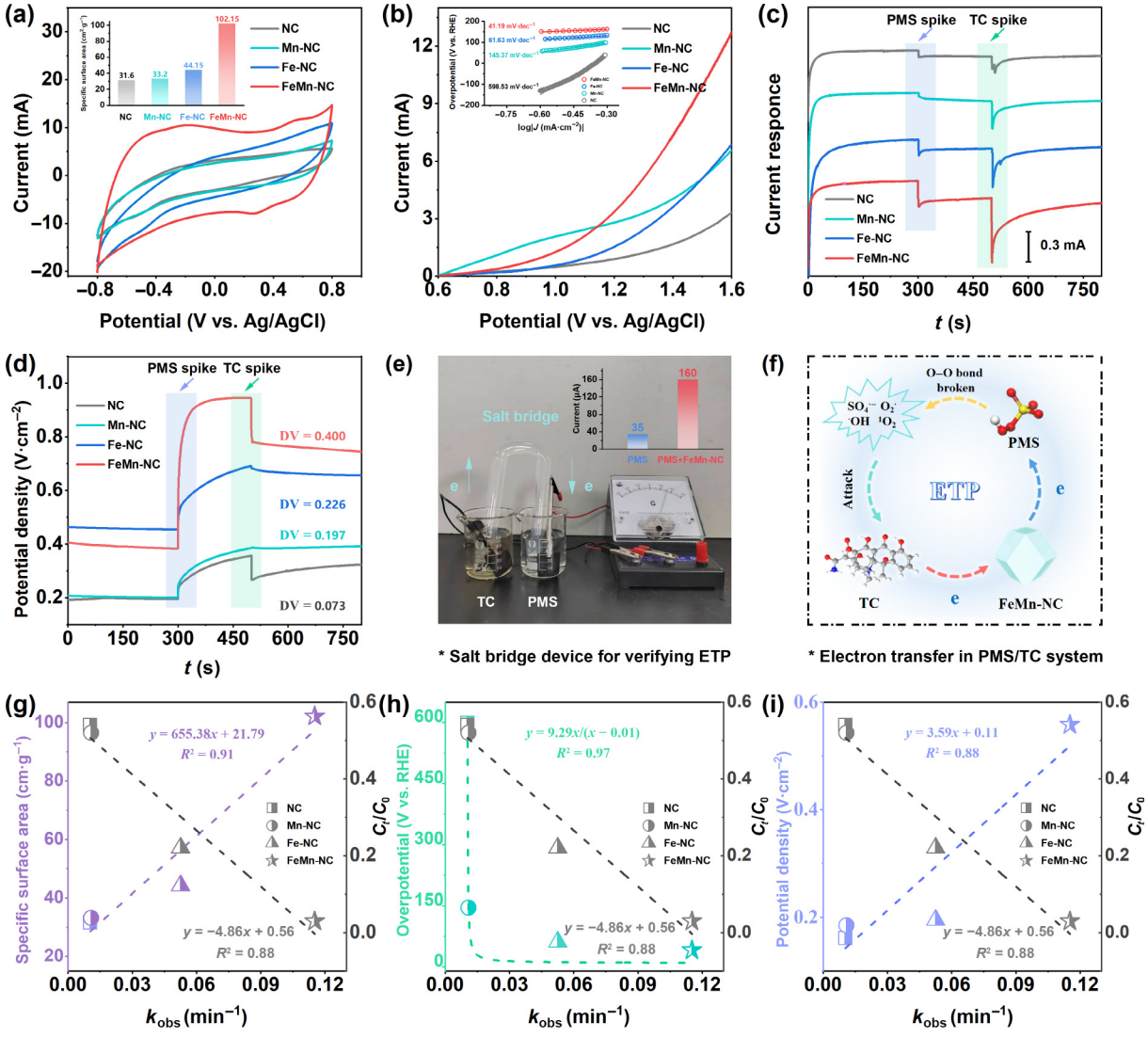


Figure 4 (a) The CV curves and (b) LSV curves of different catalysts. (c) *i*–*t* curves and (d) open-circuit potential after sequentially injecting PMS and TC. (e) Salt bridge device for verifying ETP. (f) Possible pathway of electron transfer; the linear relationship between *k* and (g) specific capacitance, degradation. (h) Current, degradation and (i) potential density, degradation.

specific scavenger, as described in Eq. (4). In contrast, a pronounced decrease in the TEMP-$^1O_2$ adduct EPR signal (Figs. 5(g)(6)) demonstrated that ·OH can be converted into $^1O_2$. The addition of L-histidine reduced both the DMPO-·OH and TEMP-$^1O_2$ EPR signals, indicating possible interconversion between ·OH and $^1O_2$. The EPR signals for both the DMPO-·OH and TEMP-$^1O_2$ adducts were suppressed upon the addition of p-BQ (Figs. 5(f)(8) and 5(g)(8)), indicating the transformation of $O_2^{\bullet-}$ into ·OH and $^1O_2$ (Eqs. (5), (6), and (9)). Under N_2-saturated conditions with p‾ BQ, the EPR signals were further suppressed (Figs. 5(f)(9) and 5(g)(9)), confirming that even in an oxygen-free environment, superoxide radicals can still convert into ·OH and $^1O_2$. Furthermore, the slightly higher pollutant degradation rate in D_2O than in H_2O provided supplementary evidence for the partial involvement of $^1O_2$ as one of the reactive oxygen species (Fig. S23 in the ESM) [42–44]. Additionally, as shown in the Figs. 5(g)(8) and 5(g)(9), in the presence of p-BQ, a small amount of $SQ^{\bullet-}$ was generated. Under aerobic conditions, $SQ^{\bullet-}$ can be converted into $O_2^{\bullet-}$ (Eq. (10)), which subsequently gave rise to $^1O_2$ (Eq. (9)). The reaction mechanisms were delineated as follows

$$PMS \xrightarrow{\text{activation}} SO_4^{\bullet-} + H_2O \rightarrow {}^{\bullet}OH \quad (3)$$

$$H_2O + {}^{\bullet}OH + SO_4^{\bullet-} \rightarrow SO_4^{2-} + H_2O_2 + H^+ \quad (4)$$

$$O_2^{\bullet-} + {}^{\bullet}OH \rightarrow {}^1O_2 + OH^- \quad (5)$$

$$DMPO - O_2^{\bullet-} \rightarrow DMPO - {}^{\bullet}OH \quad (6)$$

$$SO_4^{\bullet-} + O_2^{\bullet-} \rightarrow {}^1O_2 + SO_4^{2-} \quad (7)$$

$$O_2 \xrightarrow{SO_4^{\bullet-}\text{ accelerate}} O_2^{\bullet-} \quad (8)$$

$$O_2^{\bullet-} \rightarrow {}^1O_2 \quad (9)$$

$$P - BQ \rightarrow SQ^{\bullet-} \xrightarrow{O_2} O_2^{\bullet-} + p - BQ \quad (10)$$

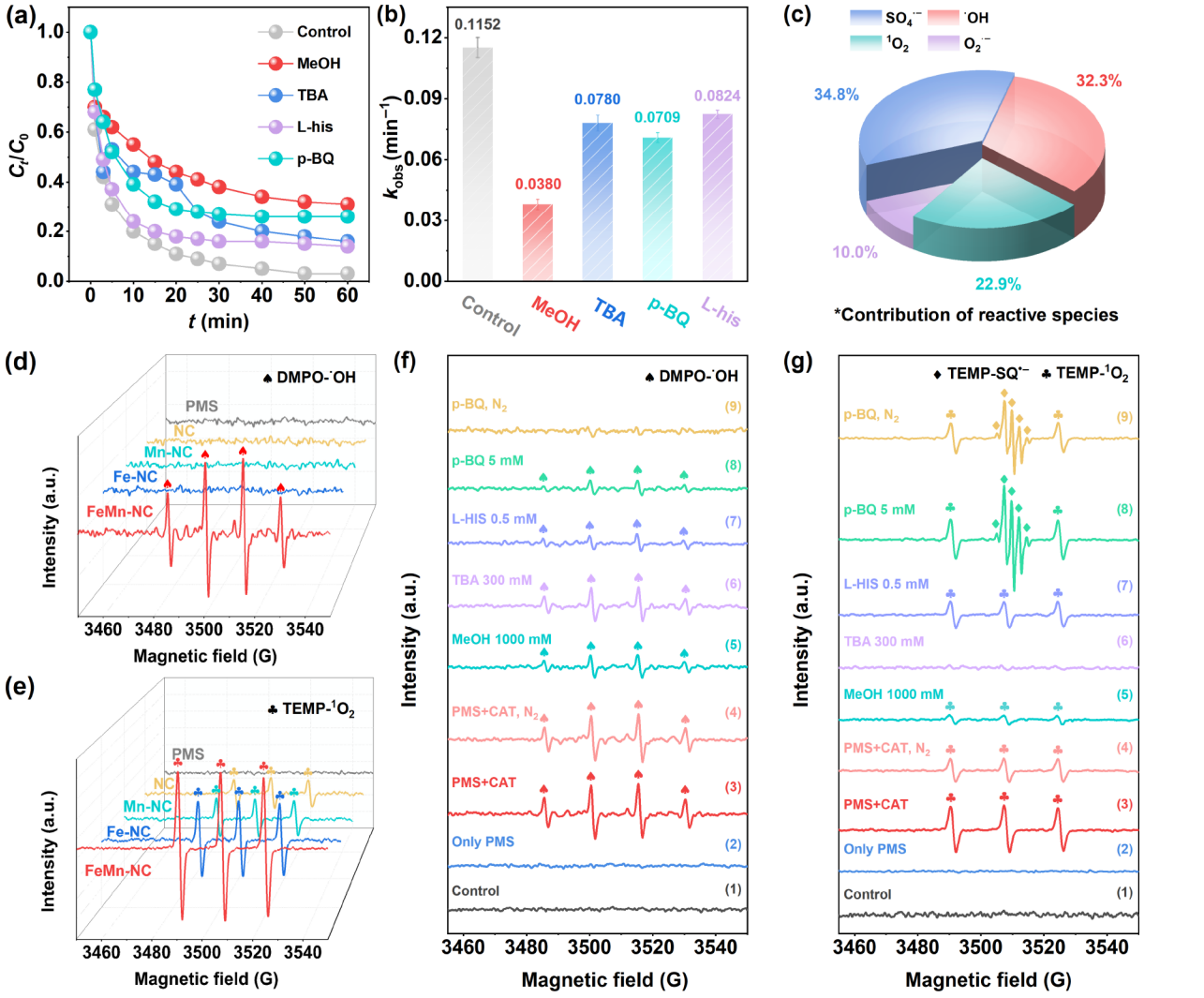


Figure 5 (a) TC removal efficiency and (b) pseudo-first-order kinetics fitting of MeOH, TBA, p-BQ, and L-histidine as the different quenching reagents. (c) Contribution of reactive species to TC removal in PMS/FeMn-NC system. EPR spectra of (d) DMPO-$^{\cdot}$OH (♠) and (e) TEPM-$^1O_2$ (♣) at the process of PMS self-decomposition or activated by different catalysts. (f) DMPO-$^{\cdot}$OH (♠) and (g) TEMP-$SQ^{\cdot-}$ (♦) and TEPM-$^1O_2$ (♣) at the process of PMS self-decomposition or activated by FeMn-NC under different reaction conditions.

3.4 DFT calculation

Figure 6(a) presented the electron localization function (ELF) maps of Fe-NC and FeMn-NC, visualizing the spatial electron localization. These findings suggested that single-atom Fe in Fe-NC significantly enhanced the electron delocalization of the catalyst, while FeMn-NC showed the highest electron delocalization among all compared systems, which stems from the concurrent presence of single-atom Fe and Fe nanoclusters [45]. This enhanced delocalization was beneficial for electron transfer during the catalytic process.

Density of states (DOS) analysis showed stronger electron state hybridization near the Fermi level in FeMn-NC compared to other catalysts (Fig. 6(b_1)). This suggested that Fe nanoclusters successfully modulated the electronic orbital configuration around single-atom Fe, thereby promoting more efficient interfacial electron transfer. Projected density of states (PDOS) analysis showed that the Fe 3d d-band center in FeMn-NC shifted to a position closer to the Fermi level (−0.96 eV) relative to that in Fe-NC (−0.99 eV, Figs. 6(b_2) and 6(b_3)). This shift suggested synergistic interactions between single-atom Fe and Fe nanoclusters, which contributed to enhanced catalytic activity. Moreover, the closer proximity of the Mn 3d orbitals to the Fermi level, compared to the Fe 3d orbitals in FeMn-NC, provided further evidence supporting the role of Fe nanoclusters in enhancing catalytic performance [46, 47].

The adsorption energy calculations demonstrated that FeMn-NC exhibited a significantly stronger adsorption energy with PMS (−2.78 eV) than other control systems (Figs. 6(c_1)–6(c_3)). This strong adsorption led to an elongation of the O–O bond length in PMS to 1.493 Å (Figs. 6(c_4)–(c_6)), which favored the decomposition of PMS. Differential charge density analysis illustrated a more pronounced electron transfer from the catalyst (blue region) to PMS (yellow region) in the PMS/FeMn-NC system (Figs. 6(c_7)–6(c_9)) [48]. Both single-atom Fe and Fe nanoclusters appeared as charge depletion zones, confirming their cooperative role in facilitating electron transfer from the FeMn-NC to PMS. Bader charge analysis confirmed the greatest electron transfer (0.92 e) in the PMS/FeMn-NC system, aligning with previous findings.

Furthermore, a correlation was established between k_{obs} of

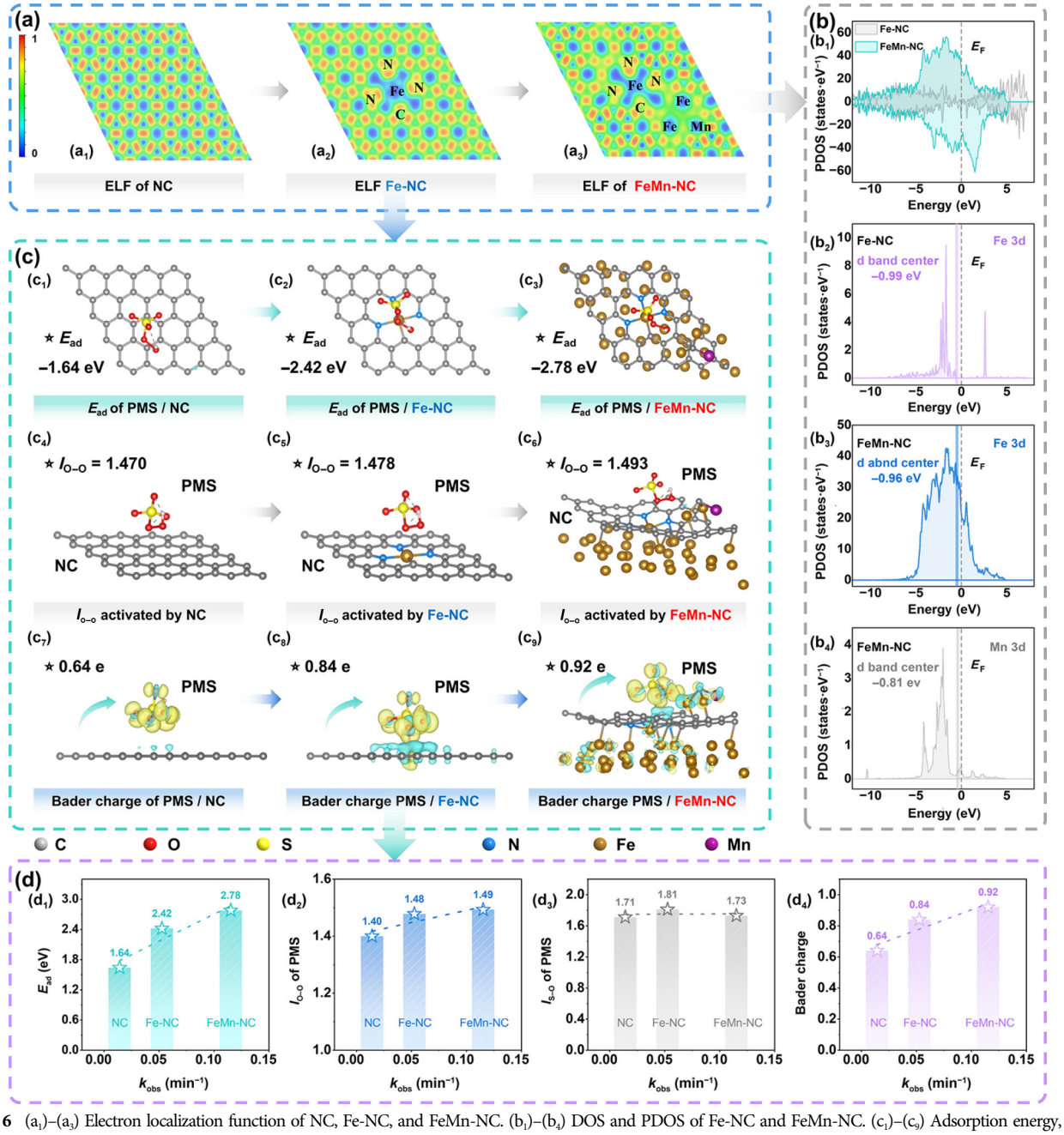


Figure 6 (a_1)–(a_3) Electron localization function of NC, Fe-NC, and FeMn-NC. (b_1)–(b_4) DOS and PDOS of Fe-NC and FeMn-NC. (c_1)–(c_9) Adsorption energy, PMS activation bond length, differential charge density, and Bader charge for NC, Fe-NC, and FeMn-NC. (d_1)–(d_4) Correlation analysis between the observed rate constant (k_{obs}) and adsorption energy, PMS activation bond length, and Bader charge for NC, Fe-NC, and FeMn-NC.

different catalysts and key theoretical parameters (Fig. 6(d)). This correlation confirmed the structure–activity relationship linking these calculated parameters to the TC degradation performance via PMS activation. In summary, this DFT investigation elucidated the synergistic Fe single-atom/nanoclusters mechanism in activating PMS from multiple perspectives, including electronic structure, adsorption behavior, and charge transfer, providing a theoretical foundation for understanding the high efficiency of this composite catalytic system.

3.5 Pollutant degradation pathways

TC initial solution exhibited distinct fluorescence signatures of fulvic-like (Region IV; Ex/Em: 250–280/280–380 nm) and humic-like substances (Region V; Ex/Em: 250-350/380-550 nm) (Fig. S25(a) in the ESM) [49]. During TC degradation, signals of organic intermediate products shifted to Region V after 5 min, accompanied by a gradual attenuation of fluorescence intensity. Figure S25(b) in the ESM summarized the calculated Fukui function values for TC, which delineated three distinct categories of reactive sites. Fukui function analysis identified three categories of reactive sites: nucleophilic centers (high f^- values), susceptible to substitution or addition; electrophilic sites (high f^+ values), prone to nitrification and halogenation; and radical-sensitive sites (high f^0 values), vulnerable to attack by $^{\cdot}OH$ and $SO_4^{\cdot-}$ [48]. The frontier molecular orbitals of TC exhibited a clear spatial separation between the highest occupied molecular orbital (HOMO)

(−6.418 eV) and the lowest unoccupied molecular orbital (LUMO) (−2.254 eV) (Fig. S25(c) in the ESM). As indicated by the LC-MS data presented in Fig. S25(d) in the ESM, distinct TC degradation mechanisms were identified within the FeMn-NC/PMS system. In Pathway I, initial deamination (A1) and deamidation (A2) were triggered by ·OH and $SO_4^{\cdot-}$, leading ultimately to A-ring cleavage (A3) mediated by $^1O_2$. Pathway II involved concurrent deamination (B1) and demethylation (B2), after which $^1O_2$ facilitated the opening of the A-ring (B3). Pathway III was initiated via radical-based deamidation (C1), followed by a combined deamination and demethylation step (C2), and terminated with $^1O_2$-promoted A-ring opening (C3).

3.6 The proposed mechanism

Figure 7 illustrated the synthesis pathway of FeMn-NC and its catalytic mechanism in the PMS system. Fe-NC contained only single-atom Fe sites (FeN_3C), whereas FeMn-NC featured a dual-active-site structure comprising single-atom Fe and Fe nanoclusters (93.17 % Fe^0 and 6.83 % $Fe_{1.8}Mn_{1.2}C$). During the one-step synthesis, the adsorption of Mn^{2+} onto Fe-ZIF and subsequent pyrolysis promoted the formation of Fe nanoclusters through two mechanisms: Carbothermal reduction of Mn^{2+} generated metallic Mn, which reduced high-valent Fe species to Fe^0, and partial substitution of carbon by Mn in the pyrolysis intermediate FeC_3 induced the formation of the $Fe_{1.8}Mn_{1.2}C$ phase. This indicated that Mn served not only as a structural promoter to facilitate nanocluster formation but also as an electronic modulator through doping, thereby enhancing electron transfer between the catalyst and PMS. Furthermore, KSCN (quenching single-atom iron sites) [50] and NaH_2PO_4 (quenching iron clusters) [51] quenching experiments clearly revealed the distinct roles of single-atom Fe sites and Fe nanoclusters in the PMS activation system (Fig. S24 in the ESM).

The dual-active-site structure endowed FeMn-NC with complementary catalytic roles. Single-atom Fe sites primarily governed a non-radical pathway, favoring $^1O_2$ generation. Fe nanoclusters enhanced PMS adsorption (Figs. 6(c1)–6(c3)), elongated the O–O bond (Figs. 6(c4) and 6(c5)), and promoted formation of $SO_4^{\cdot-}$ and $O_2^{\cdot-}$, thereby reinforcing the radical pathway (Figs. 5(d) and 5(e)). Additionally, Fe nanoclusters improved interfacial electron-transfer efficiency, as evidenced by increased ECSA, reduced Tafel slope, and a positive shift in open-circuit potential (Figs. 4(a)–4(d)). Interactions between Fe nanoclusters and single-atom Fe sites further enhanced electron delocalization (Fig. 6(a)) and shifted Fe 3d orbitals toward the Fermi level (Fig. 6(b)), facilitating electron transfer during catalysis. In summary, the synergistic interplay between single-atom Fe and Fe nanoclusters in FeMn-NC enabled concurrent non-radical and radical pathways, optimized the electronic structure of active sites, and enhanced electron-transfer efficiency, collectively improving PMS activation and overall pollutant degradation.

3.7 Environmental applications

The environmental applicability and economic viability of the PMS/FeMn-NC system were systematically evaluated. The assessment encompassed degradation efficiency of various contaminants in different water matrices, phytotoxicity assays based on wheat seed germination, and an economic analysis using the Electric Energy per Order (EE/O) method.

To assess practical potential, the influence of high ion concentration (40 mM) was investigated, revealing that dihydrogen phosphate (through competitive adsorption) [52], along with ammonium and calcium ions (via pH-related effects), influenced the degradation process [53]. Despite interfering ions, the system sustained high degradation performance for multiple pollutants, such as dyes (RhB, MB, OG) and antibiotics (TC, OTC, CTC), in real water matrices, with TC removal efficiency of 89.5% and 88.9% for tap water and river water, respectively (Figs. 8(a)–8(c)). These

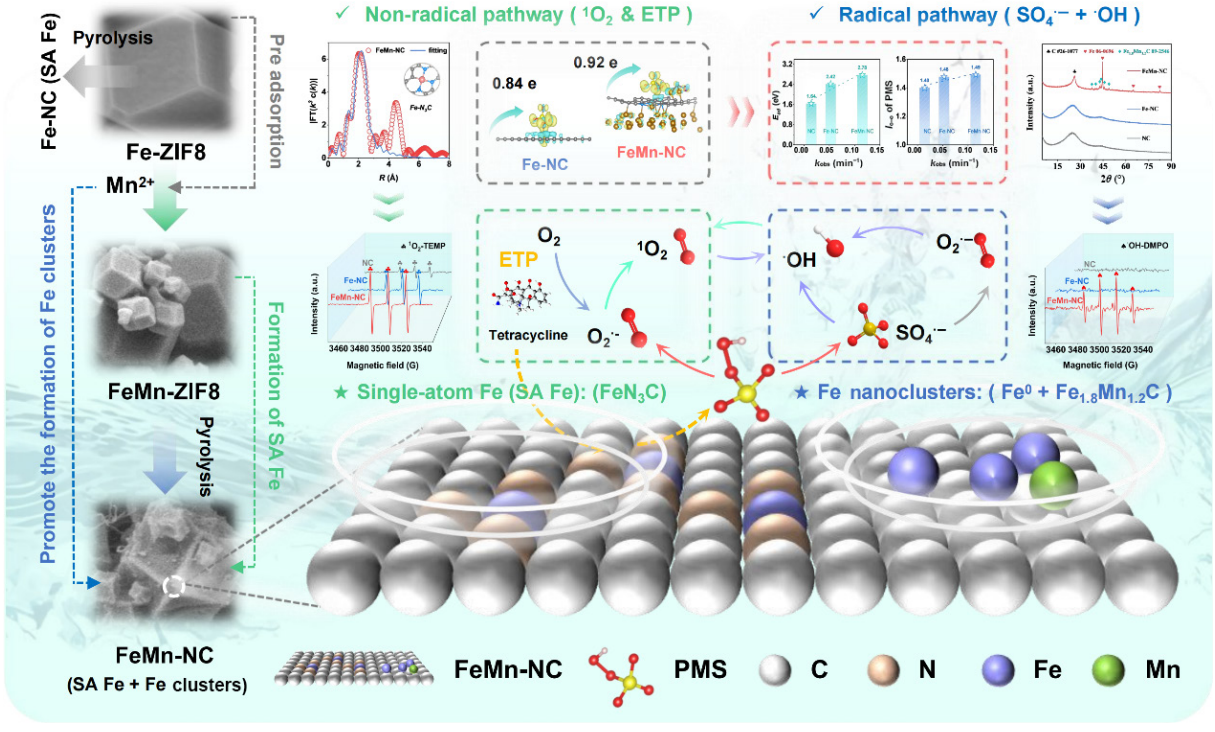


Figure 7 The proposed mechanism for the formation of active sites in FeMn-NC and the TC degradation in the PMS/FeMn-NC System.

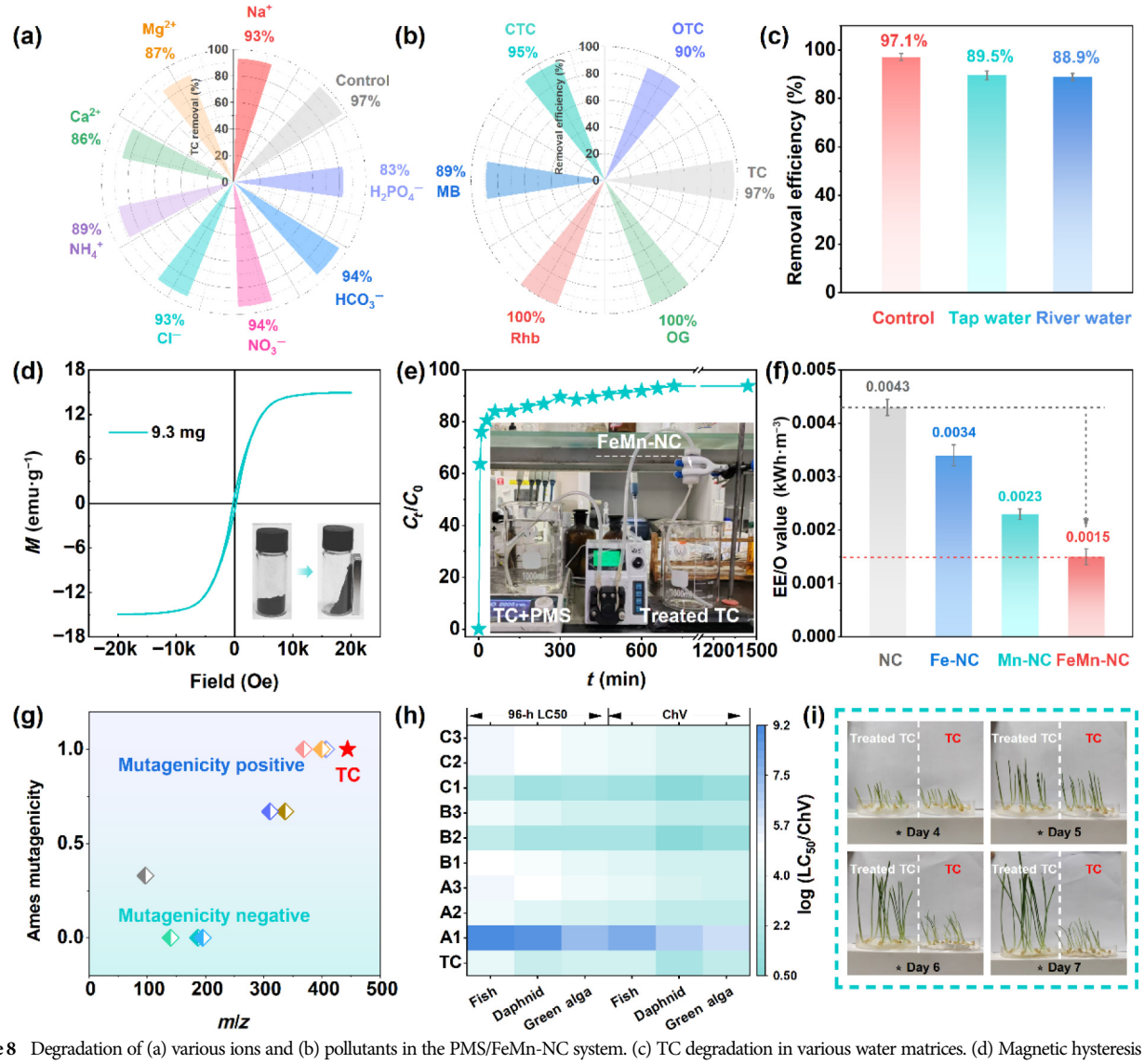


Figure 8 Degradation of (a) various ions and (b) pollutants in the PMS/FeMn-NC system. (c) TC degradation in various water matrices. (d) Magnetic hysteresis loop of FeMn-NC. (e) TC degradation over 24 h. (f) EE/O value of NC, Mn-NC, Fe-NC, and FeMn-NC. (g) Ames mutagenicity and (h) acute and chronic toxicity of intermediate products. (i) Images of wheat seeds grown in different water bodies.

results collectively demonstrated the robustness of the system and underscore its potential for practical application. Further reinforcing its practical utility, the catalyst exhibited favorable recoverability due to its magnetic properties, and demonstrated excellent operational stability by retaining over 90% degradation efficiency throughout a 24-hour continuous test (Figs. 8(d) and 8(e)). Economically, the PMS/FeMn-NC system showed a notably low EE/O value of 0.0015 kWh·m^{-3} (Fig. 8(f)), which was reduced by a factor of 2.86 relative to the PMS/NC system (0.0043 kWh·m^{-3}), highlighting its significantly reduced energy consumption—a critical advantage for scalable application [54, 55].

Toxicity assessments further supported the environmental safety of the process. TEST software predictions indicated an absence of mutagenicity for most low-molecular-weight intermediates (Fig. 8(g)). In terms of acute aquatic toxicity, the Fathead Minnow LC_{50} (Fig. S27 in the ESM) indicated reduced toxicity for most intermediates, with values distributed across a spectrum from toxic to non-toxic [56]. ECOSAR analysis indicated that most intermediates exhibited relatively low acute and chronic toxicity towards fish, Daphnia, and green algae, with the exceptions of A1, B2, and C1 (Fig. 8(h)) [57]. Consistent with these findings, the wheat seed germination test confirmed a significant reduction in the toxicity of TC after treatment (Fig. 8(i)).

4 Conclusions

In conclusion, a FeMn-NC catalyst with dual Fe sites, comprising single-atom Fe and Fe nanoclusters, was successfully developed to overcome the limitations imposed by isolated active sites in conventional SACs. The synergistic combination of these two Fe sites enabled concurrent non-radical and radical pathways during PMS activation, resulting in significantly enhanced overall catalytic performance. DFT calculations revealed that the dual-site structure strengthened PMS adsorption, elongated the O–O bond, optimized the Fe d-band center, and increased electron delocalization, collectively facilitating interfacial charge transfer. These computational insights directly correlate with the observed structural features and experimental performance of the catalyst, demonstrating that rational integration of multiple active sites can

effectively modulate reaction pathways and improve catalytic activity. This work provides a theoretical and structural basis for the design of efficient and low-cost catalysts applied in Fenton-like reactions for wastewater purification.

Electronic Supplementary Material: Supplementary material (supplementary information to support the main findings, includes 3 calculation methods (described in the text), along with 28 supplementary figures and 7 supplementary tables) is available in the online version of this article at https://doi.org/10.26599/NR.2026.94908780.

Data availability

All data needed to support the conclusions in the paper are presented in the manuscript and the Electronic Supplementary Material. Additional data related to this paper may be requested from the corresponding author upon request.

Acknowledgements

This work is granted by the National Natural Science Foundation of China (Nos. 42277194 and 42407022) and China Postdoctoral Science Foundation (Nos. GZC20232062 and 2024MD753970).

Declaration of competing interest

All the contributing authors report no conflict of interests in this work.

Author contribution statement

W. B. W.: Writing – original draft, software, methodology, formal analysis, data curation, conceptualization. T. W.: Resources. J. L.: Writing – review & editing. D. S. Z.: Data curation. C. X. L.: Software. X. H. D: Methodology. W. H. Z.: Writing – review & editing, methodology, conceptualization, funding acquisition, project administration, supervision, validation, visualization.

Use of AI statement

None.

References

[1] Yu, X. L.; Jin, X.; Li, M.; Yu, Y. Y.; Zhu, M. H.; Tang, S. Y.; Zhou, H. J.; Wang, K. F.; Dou, R. N.; Sun, J. T. Degradation mechanism of tetracycline using sulfidated nanoscale zerovalent iron driven peroxymonosulfate and metabolomic insights into environmental risk of intermediates products. *Chem. Eng. J.* **2022**, *430*, 133141.

[2] Yi, Q. Z.; Gao, Y. X.; Zhang, H.; Zhang, H. F.; Zhang, Y.; Yang, M. Establishment of a pretreatment method for tetracycline production wastewater using enhanced hydrolysis. *Chem. Eng. J.* **2016**, *300*, 139–145.

[3] Barranco-López, A.; Moral-Rodríguez, A. I.; Fajardo-Puerto, E.; Elmouwahidi, A.; Bailón-García, E. Highly graphitic Fe-doped carbon xerogels as dual-functional electro-Fenton catalysts for the degradation of tetracycline in wastewater. *Environ. Res.* **2023**, *228*, 115757.

[4] Chen, J. B.; Xu, J.; Liu, T. C.; Qian, Y. J.; Zhou, X. F.; Xiao, S. Z.; Zhang, Y. L. Selective oxidation of tetracyclines by peroxymonosulfate in livestock wastewater: Kinetics and non-radical mechanism. *J. Hazard. Mater.* **2020**, *386*, 121656.

[5] Zhao, Y. L.; Wu, T.; Du, X. H.; Shi, Q. Y.; Feng, Y. Z.; Zhu, W. H. Multifunctional biochar cathode engineered with coarse tea extract assistance for water purification: Simultaneous H_2O_2 generation, ferrous regeneration, and dissolution inhibition. *Appl. Surf. Sci.* **2026**, *727*, 165934.

[6] Xia, H. L.; Li, C. W.; Yang, G. Y.; Shi, Z. A.; Jin, C. X.; He, W. Z.; Xu, J. C.; Li, G. M. A review of microwave-assisted advanced oxidation processes for wastewater treatment. *Chemosphere* **2022**, *287*, 131981.

[7] Qi, M. Y.; Lin, P.; Shi, Q. Y.; Bai, H. L.; Zhang, H.; Zhu, W. H. A metal-organic framework (MOF) and graphene oxide (GO) based peroxymonosulfate (PMS) activator applied in pollutant removal. *Process Saf. Environ. Prot.* **2023**, *171*, 847–858.

[8] Li, J. L.; Zhu, W. H.; Gao, Y.; Lin, P.; Liu, J. W.; Zhang, J. F.; Huang, T. L. The catalyst derived from the sulfurized Co-doped metal-organic framework (MOF) for peroxymonosulfate (PMS) activation and its application to pollutant removal. *Sep. Purif. Technol.* **2022**, *285*, 120362.

[9] Xie, F. S.; Zhu, W. H.; Lin, P.; Zhang, J. B.; Hao, Z. L.; Zhang, J. F.; Huang, T. L. A bimetallic (Co/Fe) modified nickel foam (NF) anode as the peroxymonosulfate (PMS) activator: Characteristics and mechanism. *Sep. Purif. Technol.* **2022**, *296*, 121429.

[10] Shi, Q. Y.; Zhu, W. H.; Wang, W. B.; Xie, F. S.; Feng, Y. Z. Nitrogen-containing biochar derived from bean dregs as catalyst for peroxymonosulfate-based Fenton-like reactions: Synergistic effects of cobalt encapsulation and boron doping. *Chem. Eng. J.* **2025**, *517*, 164407.

[11] Wang, J. L.; Tang, J. T. Fe-based Fenton-like catalysts for water treatment: Preparation, characterization and modification. *Chemosphere* **2021**, *276*, 130177.

[12] Wang, W. B.; Shi, Q. Y.; Wu, T.; Zheng, S. S.; Xu, Z. Y.; Zhu, W. H. Fe/S co-doped biochar catalysts for enhanced peroxymonosulfate activation: Synergistic effects of catalysis and anti-deactivation on antibiotic degradation. *J. Cleaner Prod.* **2025**, *533*, 147005.

[13] Xi, J. B.; Jung, H. S.; Xu, Y.; Xiao, F.; Bae, J. W.; Wang, S. Synthesis strategies, catalytic applications, and performance regulation of single‐atom catalysts. *Adv. Funct. Mater.* **2021**, *31*, 2008318.

[14] Li, D. H.; Zhang, S. X.; Li, S. N.; Tang, J. C.; Hua, T.; Li, F. X. Mechanism of the application of single-atom catalyst-activated PMS/PDS to the degradation of organic pollutants in water environment: A review. *J. Cleaner Prod.* **2023**, *397*, 136468.

[15] Wang, X. C.; Kang, Z. W.; Wang, D.; Zhao, Y. F.; Xiang, X.; Shang, H. S.; Zhang, B. Electronic structure regulation of the Fe-based single-atom catalysts for oxygen electrocatalysis. *Nano Energy* **2024**, *121*, 109268.

[16] Gao, Y. W.; Zhu, Y.; Li, T.; Chen, Z. H.; Jiang, Q. K.; Zhao, Z. Y.; Liang, X. Y.; Hu, C. Unraveling the high-activity origin of single-atom iron catalysts for organic pollutant oxidation via peroxymonosulfate activation. *Environ. Sci. Technol.* **2021**, *55*, 8318–8328.

[17] Zhang, S. Q.; Lu, Z. C.; Hu, C.; Li, F. Understanding the distance effect of the single‐atom active sites in Fenton‐like reactions for efficient water remediation. *Adv. Sci.* **2024**, *11*, 2307151.

[18] Dai, H. W.; Hu, T.; Zhu, S. Y.; Zhang, Y. J.; Zhou, W. J. Regulating the Fe–N_x coordination structure of Fe single-atom catalysts for efficient catalytic degradation of methylparaben. *Chem. Eng. J.* **2025**, *507*, 160462.

[19] Liu, Y. Q.; Zhang, G. B.; He, T.; Zhao, E. Z.; Zhao, S. Y.; Yang, S. X.; Niu, J. F. Planar-axial synergistic modulation of FeSA–O/P-NC single-atom catalyst for high-efficiency PMS activation in sulfonamides degradation. *Appl. Catal. B: Environ. Energy* **2026**, *382*, 125967.

[20] Wu, Z. L.; Huang, B. K.; Wang, X. H.; He, C. S.; Liu, Y.; Du, Y.; Liu,

W.; Xiong, Z. K.; Lai, B. Facilely tuning the first-shell coordination microenvironment in iron single-atom for Fenton-like chemistry toward highly efficient wastewater purification. *Environ. Sci. Technol.* **2023**, *57*, 14046–14057.

[21] Jeong, H.; Shin, S.; Lee, H. Heterogeneous atomic catalysts overcoming the limitations of single-atom catalysts. *ACS Nano* **2020**, *14*, 14355–14374.

[22] Gu, L.; Cao, X.; Yang, H. Y.; He, Y. Y.; Wang, X.; Wen, H. F.; Zhang, H. L.; Xu, S. Y.; Yuan, H. P.; Hu, K. Tailoring peroxyacetic acid (PAA) activation by sewage sludge derived atomic-Fe clusters/Fe-N_4 catalyst via thermally driven spin manipulation. *J. Colloid Interface Sci.* **2025**, *686*, 251–266.

[23] Fan, M. Y.; Zhang, T. R.; Gao, Z. K.; You, S. Y.; Shang, Y. A.; Peng, X. M.; Geng, L. L.; Wang, Y. F.; Liu, M. L.; Xu, X. Synergistic architectures in Fenton-like catalysis: Bridging single-atom and nanoparticle/cluster dynamics for enhanced activity, stability, and selectivity. *Adv. Funct. Mater.* **2025**, *35*, 2508484.

[24] Zeng, H. X.; Che, Y. B.; Yang, B. F.; Deng, J.; Zhang, C. Y.; Wang, J.; Zhang, H. J. Differential catalytic mechanism induced by selective adsorption of pollutants in metal clusters decorated single atom catalyst mediated heterogeneous Fenton-like reaction. *J. Hazard. Mater.* **2025**, *491*, 138029.

[25] Li, C. Y.; Kang, L.; Wang, S.; Gao, B.; Gao, X. Q.; Shi, W. J.; Ai, S. Y.; Wu, J. C.; Sun, Y. Y. Enhanced PFOA degradation via non-radical PMS pathway through synergistic Fe single-atoms and Fe nanoparticles in Fe–N–C catalysts. *Chem. Eng. J.* **2025**, *512*, 162424.

[26] Zhao, M. D.; Xu, Z. B.; Duan, X. G.; Graham, N. J. D.; Zhong, H.; Tsang, D. C. W. Collaborative catalysis of single atoms and atomic clusters as dual sites for confined peroxymonosulfate activation to coordinate radical and singlet oxygen pathways. *Water Res.* **2026**, *288*, 124655.

[27] Hu, Y. H.; Guo, H.; Lv, Y. C.; Tian, C.; Lin, Y. L.; Liu, H. Axial enhancement on non-radicals generation in PMS activation process mediated with Co single-atom catalyst encapsulated nanoparticles. *J. Hazard. Mater.* **2025**, *496*, 139513.

[28] Li, Y. Y.; Jiang, H. M.; Lin, L.; Sun, Z. M.; Sun, G. B. Single-atomic iron synergistic atom-cluster induce remote enhancement toward oxygen reduction reaction. *J. Energy Chem.* **2025**, *102*, 413–420.

[29] Xie, F. S.; Shi, Q. Y.; Bai, H. L.; Liu, M. Y.; Zhang, J. B.; Qi, M. Y.; Zhang, J. F.; Li, Z. H.; Zhu, W. H. An anode fabricated by Co electrodeposition on ZIF-8/CNTs/CF for peroxymonosulfate (PMS) activation. *Chemosphere* **2023**, *313*, 137384.

[30] Xu, Z. Y.; Wu, T.; Feng, Y. Z.; Zhang, Y. X.; Hou, T.; Yun, S. N.; Li, Z. H.; Zhu, W. H. Fabrication of a highly efficient and stable peroxymonosulfate activator via a new sequential adsorption-encapsulation strategy induced by metal-organic framework. *J. Environ. Chem. Eng.* **2025**, *13*, 115495.

[31] Yang, Z. Y.; Yang, X. F.; An, G. Y.; Wang, D. S. Regulating spin state of Fe active sites by the P-doping strategy for enhancing peroxymonosulfate activation. *Appl. Catal. B: Environ.* **2023**, *330*, 122618.

[32] Zhang, L.; Sun, Y.; Ge, R. L.; Zhou, W. H.; Ao, Z. M.; Wang, J. H. Mechanical insight into direct singlet oxygen generation pathway: Pivotal role of FeN_4 sites and selective organic contaminants removal. *Appl. Catal. B: Environ.* **2023**, *339*, 123130.

[33] Yadav, A.; Yadav, P.; Labhasetwar, P. K.; Shahi, V. K. CNT functionalized ZIF-8 impregnated poly(vinylidene fluoride-co-hexafluoropropylene) mixed matrix membranes for antibiotics removal from pharmaceutical industry wastewater by vacuum membrane distillation. *J. Environ. Chem. Eng.* **2021**, *9*, 106560.

[34] Li, Z. L.; Deng, L. B.; Kinloch, I. A.; Young, R. J. Raman spectroscopy of carbon materials and their composites: Graphene, nanotubes and fibres. *Prog. Mater. Sci.* **2023**, *135*, 101089.

[35] Al-Ghouti, M. A.; Da'ana, D. A. Guidelines for the use and interpretation of adsorption isotherm models: A review. *J. Hazard. Mater.* **2020**, *393*, 122383.

[36] Song, Y. N.; Feng, Y. Z.; Wu, T.; Yang, R.; Shi, Q. Y.; Yi, Z.; Li, Z. H.; Zhu, W. H. Boosted adsorption and oxidation performances in peroxymonosulfate (PMS)-based heterogeneous fenton-like reactions via P, N co-doping strategy. *Sep. Purif. Technol.* **2025**, *354*, 128587.

[37] Shi, Q. Y.; Feng, Y. Z.; Wang, W. B.; Xu, Z. Y.; Li, Z. H.; Zhu, W. H. Porous biochar encapsulating highly dispersed Co_3O_4 as peroxymonosulfate activator for the enhanced tetracycline removal. *Process Saf. Environ. Prot.* **2025**, *196*, 106947.

[38] Xie, F. S.; Yang, R.; Weng, S. F.; Zhang, Y. X.; Hou, T.; Zhang, J. F.; Li, Z. H.; Zhu, W. H. Enhancement of anodic performance toward peroxymonosulfate-based fenton-like reactions: Role of phosphorus-doping. *Chem. Eng. J.* **2025**, *505*, 159588.

[39] Xu, Z. Y.; Feng, Y. Z.; Wu, T.; Shi, Q. Y.; Wang, W. B.; Li, Z. H.; Zhu, W. H. An efficient peroxymonosulfate activator derived from metal-organic frameworks: The application of Cu, Mg co-doping strategy. *J. Environ. Chem. Eng.* **2024**, *12*, 114369.

[40] Gao, W. Y.; Cao, X. Q.; Hou, L. F.; Lu, H. Y.; Zhu, Z. J.; Kong, W. J.; Zhang, Y.; Zhang, Y. Z.; Shang, Y. N.; Xu, X. Electron transfer chemistry triggered by silicon-doped carbon catalysts derived from natural minerals for the degradation of organic pollutants. *Chin. Chem. Lett.* **2026**, *37*, 111095.

[41] Yang, R.; Zhang, X. J.; Xu, Z. Y.; Weng, S. F.; Xie, F. S.; Zhu, W. H. Application of anodic driven and bimetallic doping strategies in peroxymonosulfate-based Fenton-like reactions. *Sep. Purif. Technol.* **2025**, *354*, 129398.

[42] Huang, J. Z.; Zhang, H. C. Redox reactions of iron and manganese oxides in complex systems. *Front. Environ. Sci. Eng.* **2020**, *14*, 76.

[43] Tong, J. T.; Xu, W. H.; Bai, S.; Zhao, X. H.; Qian, J. "P-strengthening strategy" of nickel single-atom catalyst with boosting selective generation of nonradicals: Synergy of metal center and substrate. *Adv. Funct. Mater.* **2025**, *35*, 2508487.

[44] Qian, J.; Bai, S.; Ma, R.; Tong, J. T.; Du, H. Y.; Yin, W. J.; Dong, H. R.; Zhan, S. H. Asymmetrically coordinated nickel single-atom catalyst optimizes electron transfer for ultra-efficient wastewater purification. *Appl. Catal. B: Environ. Energy* **2026**, *389*, 126567.

[45] Zhang, S. Y.; Sun, B. W.; Liao, K.; Wang, X.; Chen, Z. Y.; Wang, J. J.; Hu, W. B.; Han, X. P. Boosting oxygen reduction reaction performance of Fe single-atom catalysts via precise control of the coordination environment. *Adv. Funct. Mater.* **2025**, *35*, 2425640.

[46] Xiong, M.; Li, S.; Bi, Z. Y.; Liu, P.; Xue, W. X.; Dai, J. H.; Xi, J. B. Boosting hydrogen transfer catalysis by symmetry breaking of iron site. *Appl. Catal. B: Environ. Energy* **2026**, *385*, 126320.

[47] Wu, C.; Jia, S. B.; Zhu, H. Y.; Shang, J. X.; Li, T. T.; Chen, S. L.; Ren, Z. Q.; Meeladi, G.; Suo, B. B.; Zou, W. L. et al. d-s/p orbital hybridization-driven synergy in heteronuclear dual-atom catalysts on CN/C_2N for high-efficiency lithium-sulfur batteries. *Carbon* **2026**, *246*, 120862.

[48] Wang, W. B.; Yang, R.; Li, T.; Wu, T.; Shi, Q. Y.; Feng, Y. Z.; Li, Z. H.; Gao, Y.; Zhu, W. H. The catalyst derived from MoS_2 with Fe/Cu dual-active-sites for peroxymonosulfate activation in antibiotic degradation: The role of Fe and Cu co-doping strategy. *Chem. Eng. J.* **2025**, *526*, 171037.

[49] Hu, J. Q.; Tian, J. L.; Yang, Y.; Li, S. S.; Lu, J. F. Enhanced antibiotic degradation via photo-assisted peroxymonosulfate over graphitic carbon nitride nanosheets/$CuBi_2O_4$: Highly efficiency of oxygen activation and interfacial charge transfer. *J. Colloid Interface Sci.* **2024**, *661*, 68–82.

[50] Jin, S. J.; Tan, W. X.; Huang, Y. L.; Wang, Y.; He, Z. Q.; Zhang, H. Y.; Song, S.; Cai, Y. Q.; Zeng, T. Remote tuning of single-atom

Fe–N_5 sites via high-coordination defects for enhanced Fenton-like water decontamination. *Nat. Commun.* **2025**, *16*, 10455.

[51] Loukoutos, N.; Sciscenko, I.; Minella, M.; Vione, D.; Katsoyiannis, I. A. Enhanced degradation of phenol via a zero-valent iron-sodium percarbonate (ZVI-SPC) Fenton-like system: Toward environmentally relevant water treatment conditions. *J. Environ. Chem. Eng.* **2026**, *14*, 121511.

[52] Li, Z. X.; Huo, Y.; Li, T. R.; Dong, S. S.; Huo, M. X.; Liu, G.; Sun, M. Toward practical water decontaminations via peroxymonosulfate nonradical oxidation: The role of cocatalyst MoS_2 with sulfur vacancies. *ACS EST Eng.* **2023**, *3*, 1975–1985.

[53] Yan, Z. L.; He, F.; Zhang, J. Y.; Fang, J. R.; Wang, J. J.; Zhou, H. H. Enhanced Fe(Ⅲ)/PMS system by flower-like MoS_2 nanosheet for rapid degradation of tetracycline. *J. Environ. Chem. Eng.* **2022**, *10*, 108860.

[54] Dai, Q.; Yu, G. F.; Qi, J. J.; Wang, Y. N.; Xing, L.; Wang, Y. H.; Zhang, Z. J.; Zhong, X. L.; Fang, Z. M.; Du, P. H. et al. Ternary Co-O_v-Cu sites trigger Co-utilization of endogenous electron donor-acceptor for sustainable removal of refractory low-carbon fatty amines in Fenton-like system. *Appl. Catal. B: Environ.* **2024**, *340*, 123184.

[55] Dai, Q.; Li, Z. H.; Zhong, X. L.; Wang, Y. X.; Qi, J. J.; Wang, Y. A.; Fang, Z. M.; Xing, L.; Li, Z.; Wang, L. D. Preventing re-emission of malodorous dimethylamine via tunable nonradical oxidation catalyzed by waste mask-derived carbocatalyst. *Chem. Eng. J.* **2022**, *450*, 138510.

[56] Yang, Z. Z.; Tan, X. F.; Zhang, C. Sulfidation of Ni-Fe-LDH for enhanced Fenton-like catalysis: Experimental validation and theoretical calculation. *Sep. Purif. Technol.* **2024**, *336*, 126320.

[57] Liang, Y. L.; Feng, A. C.; Al-Dhabi, N. A.; Zhang, J.; Xing, W. L.; Chen, T.; Han, Y. X.; Zeng, G. M.; Tang, L.; Tang, W. W. Efficient antibiotic tetracycline degradation and toxicity abatement via the perovskite-type $CaFe_xNi_{1-x}O_3$ assisted heterogeneous electro-Fenton system. *Water Res.* **2025**, *279*, 123432.

This is an open access article under the terms of the Creative Commons Attribution 4.0 International License (CC BY 4.0, https://creativecommons.org/licenses/by/4.0/).

© The Author(s) 2026. Published by Tsinghua University Press.